



A dynamic structure evolution and reaction pathway over Ni₂P for enhancement toward furfural oxidation

Zhikun Peng^a, Siying Li^a, Rui Li^a, Kaihang Sun^a, Jianpeng Li^{a,*}, Yanyan Liu^{c,d}, Zhongyi Liu^a, Yongjing Wang^b, Jingmin Ge^{a,*}, Kun Xiang^{b,*}

^a Henan Institute of Advanced Technology, Green Catalysis Center, College of Chemistry, School of Mechanics and Safety Engineering, Zhengzhou University, Zhengzhou 450001, PR China

^b School of Chemistry and Environmental Engineering, School of Environmental Ecology and Biological Engineering, Wuhan Institute of Technology, Wuhan 430205, PR China

^c College of Science, Henan Agricultural University, 63 Agriculture Road, Zhengzhou 450002, PR China

^d Institute of Chemical Industry of Forest Products, CAF, National Engineering Lab. for Biomass Chemical Utilization, 16 Suojinwucun, Nanjing 210042, PR China



ARTICLE INFO

Keywords:

Ni₂P-Ni(OH)₂

Dynamic structure evolution

Furfural electrooxidation

ABSTRACT

The electrocatalytic conversion of furfural (FF) holds a great promise for value-added furoic acid (FA) generation. However, the dynamic evolution of the catalyst surface during the reaction has seriously hindered our comprehensive understanding of the catalytic process and mechanism. In this paper, we discovered active phase over Ni₂P strongly depends on the applied potential. Specifically, Ni₂P serves as active phase at 1.30–1.40 V_{RHE} and FOR occurs in a direct way. While the in-situ formed single oxide layer of Ni₂P-Ni(OH)₂ heterostructure from surface reconstruction dramatically enhances FOR in an indirect way at 1.40–1.60 V_{RHE}, resulting in 85 % FA selectivity and 87 % faradaic efficiency (FE) after deducting FF Cannizzaro reaction. After exceeding 1.60 V_{RHE}, OER will have strong competition with the Ni(OH)₂ formation. The proposed dynamic heterostructure model of Ni₂P-Ni(OH)₂ derived from Ni₂P has been validated for its universality to other X-ides (NiS and NiSe₂) for FOR and other nucleophilic reagents.

1. Introduction

The catalytic conversion of biomass-based molecules to produce high-value chemicals and fuels has important applications in medicine, industry and agriculture, accelerating the achievement of social goals of sustainable development [1–6]. Catalytic reactions induced by heat, light, electricity, and photoelectricity, and more and more representative systems for each of them are being explored and consolidated. Among them, upgrading biomass-based molecules (such as aldehydes, alcohols, amines and lipids, etc.) into high-value products through electrocatalytic oxidation reactions has been investigated for decades and is becoming more and more popular [7–13]. Attribute to the electricity generated by renewable energy drives nucleophiles electrocatalytic oxidation to produce high-value products, which has the advantages of high selectivity, low energy consumption and economic feasibility [14–19]. Moreover, the nucleophile oxidation reaction (NOR) of organic biomass-based molecules and the successful coupling of HER achieve the value-added refining of organic molecules and hydrogen

production. It has become an important direction in the field of electrocatalysis and electrosynthesis at present. [20–29].

In the conventional sense, the catalysts used in thermal catalytic reactions are relatively stable after high temperature treatment, and may be able to maintain the corresponding structure and active site under reaction conditions. Many efforts have been focused on the design and synthesis of fresh catalysts and their structure-activity relationship. However, in the field of electrocatalytic reactions, the purpose of seeking to improve the intrinsic active site of the catalyst (such as the active site structure or the number of active sites) may fail, due to the reconstruction of the catalysts during the application of a voltage. [30–32]. This can lead to the futility of putting effort into designing catalysts that remain unchanged throughout the whole potential process to improve the catalyst activity. Or the high activity of the catalyst is attributed to the unrealistic catalyst active site, resulting in the wrong structure-activity relationship. [33–35]. Versatile non-noble metal electrocatalysts such as phosphide, sulf-ide, nitr-ide, selen-ide, and car-ide (denoted as metal X-ide) have shown extraordinary performance

* Corresponding authors.

E-mail addresses: lijianpeng4131@163.com (J. Li), yhgejingmin@163.com (J. Ge), xiangkun@wit.edu.cn (K. Xiang).

for both NOR and HER in alkaline electrolytes. [36]. However, metal X-ides are difficult to host the real active sites due to their thermodynamic instability during NOR process, and it has been reported that the metal X-ides can be electrochemically oxidized and transformed into corresponding oxides and (oxy)hydroxides. Besides, due to the competitive reaction between NOR and OER, and there is inevitable potential-dependent overpotential overlaps between the nucleophile molecules oxidation and OER. Given that NOR process involves both the catalysts structure evolution inducing the active site changes and the competitive reaction between NOR and OER, the exploration of the mechanism and reaction pathway is trapped in a developmental dilemma, and revealing the dynamic structure evolution of catalysts and identifying competitive reactions has become a daunting challenge. However, most NOR reactions are complicated, for example, the oxidation of ethanol to acetic acid requires four-step proton coupled electron transfer (PCET) process and one-step hydration; the oxidation of 5-Hydroxymethyl-2-furaldehyde to 2,5-Furandicarboxylic acid requires six-step PCET process and two-step hydration; the oxidation of urea to nitrogen and carbon dioxide requires six-step PCET process, one-step hydration and one-step rearrangement. But the oxidation process of the furfural is simple, involving only two-step PCET and one-step hydration [37]. Besides, FF is a platform molecule derived from biomass, that can be used to synthesize high-value industrial chemicals through a series of chemical reactions. And the main oxidation product FA is an important raw material for medicine, pesticide and perfume industry [20]. So that it is very suitable for study the evolution of the catalysts during the process. Among the Ni X-ide catalysts, phosphides deserve particular recognition due to their low cost, natural abundance and great catalytic activity [38,39]. Besides, the high conductivity properties of phosphide make it kinetically favorable for rapid electron transfer [40]. So we choose the Ni₂P with the research object of this paper is suitable.

Herein, in order to study the structure evolution and corresponding reaction pathways over Ni X-ide in the whole applied potential during electrocatalytic NOR, Ni₂P and FF are selected as the model catalyst and nucleophile, respectively. The results demonstrated three-step evolution process occurs over Ni₂P during furfural oxidation reaction (FOR). Firstly, Ni₂P serves as active phase directly electrooxidized FF to FA via the surface adsorbed OH* at 1.30–1.40 VRHE. Secondly, the surface reconstruction of Ni₂P occurred and in-situ formed Ni₂P-Ni(OH)₂ heterostructure significantly enhanced FOR without competition of OER via an indirect reaction pathway at 1.40–1.60 VRHE. A dynamic circle of Ni₂P-Ni(OH)₂ and Ni₂P-Ni(OH)O is formed during FF dehydrogenation to FA. Thirdly, when the potential is beyond 1.60 VRHE, the OER is gradually enhanced with the Ni(OH)O accumulation and Ni(OH)₂ formation. the dynamic heterostructure of Ni₂P-Ni(OH)₂ evolved from Ni₂P has been verified for its universality to other metal X-ides for FOR (eg. NiS and NiSe₂). Also, Ni₂P exhibits the same potential-dependent performance characteristics to other nucleophilic reagents. This work provides insights to the dynamic structure evolution and the potential competition reaction paths of the electro-oxidation systems, and more importantly, provide guidance for us to design the high-performance catalysts.

2. Experimental section

2.1. Materials and reagents

Hydrochloric acid (HCl, >37 %), ethanol (>99.7 %), nickel nitrate hexahydrate (Ni(NO₃)₂ 6H₂O), urea, ammonium fluoride (NH₄F), sodium hypophosphite (NaH₂PO₂), potassium hydroxide (KOH), furfural (FF), and furoic acid (FA) were purchased from Aldrich (China). All of the reagents were used without any purification. Nickel foam (NF) was provided by HGP.

2.2. Pre-treatment of nickel foam

The pre-cleaned Nickel foam (NF) was obtained via ultrasonication of 3 M HCl solution, ethanol, and deionized water, respectively.

2.3. Preparation of Ni(OH)₂/NF precursor

As for Ni(OH)₂ precursor synthesis, firstly, 3 mmol Ni(NO₃)₂ 6H₂O, 5 mmol NH₄F, and 5 mmol urea were dissolved in 30 mL deionized water and stirred for 30 min to obtain homogeneous solution. Then, the mixed solution was transferred into 50 mL Teflon-lined autoclave and a pieces of pre-cleaned Nickel foam (NF) was immersed for subsequent hydrothermal reaction at 120 °C for 6 h. The NF was cleaned by 3 M HCl solution, ethanol, and deionized water for 20 min ultrasound treatment, respectively. Then obtained Ni(OH)₂/NF was thoroughly rinsed with water and ethanol, followed by drying under vacuum at 60 °C for 6 h.

2.4. Preparation of Ni₂P/NF nanoflowers

As for Ni₂P nanoflowers preparation, a tube furnace was used, where 1.0 g NaH₂PO₂ was placed on the upstream side and the as-synthesized Ni(OH)₂ precursor was placed on the downstream side. Before the furnace was heated to 300 °C with a heating rate of 10 °C min⁻¹ and maintained for 1 h under Ar atmosphere, it was purged with Ar gas for 30 min. Subsequently, the black Ni₂P nanoflowers was obtained after cooling down to room temperature.

2.5. Preparation of Ni₂S Se /NF catalyst for comparison

It is similar to Ni₂P/NF synthesis, NaH₂PO₂ was replaced with S powders and Se powders, respectively.

2.6. Electrochemical measurement

The electrochemical measurements were measured on CHI660E electrochemical work station using a conventional three-electrode system at the room temperature. The synthesized Ni₂P/NF was directly used as working electrode, while graphite rod and saturated Ag/AgCl were served as the counter electrode and referenced electrode, respectively. All electrochemical measurement was conducted in a H-cell separated with Nafion 117 membrane, and 1.0 M KOH with/without 50 mM FF were used as catholyte and anolyte, respectively. It is stated that all potentials in this work were referenced to reversible hydrogen electrode (RHE), which follows such equation: E_{RHE}. The potential compensated with 90 % iR has been pointed, otherwise it is not compensated.

3. Results and discussion

3D self-supported Ni₂P nano-flower-like electrocatalyst was successfully synthesized with a two-step method involved hydrothermal reaction and subsequent phosphorization (details in [supporting information](#)). The precursor of Ni(OH)₂ nanosheet and the nano-flower Ni₂P is characterized by X-ray diffraction (XRD) and the results are depicted in [Fig. 1a](#). Apparently, the precursor exhibits the diffraction angles of 20 = 19.5°, 33.4°, 38.8°, and 59.3°, which correspond to the crystal planes of (001), (100), (101), and (111) for Ni(OH)₂ (PDF#03-0177), respectively. After the phosphating reaction, the representative peaks of the as-obtained material at positions 40.8, 47.3, and 54.2° represent the (111), (210), and (211) planes for Ni₂P (PDF#74-1485), respectively, demonstrating successful phosphating of Ni(OH)₂.

The morphology and structural details of the samples are determined by scanning electron microscopy (SEM) and high-resolution transmission electron microscopy (HRTEM). [Fig. 1b](#) and c show that the nano-flower Ni₂P is uniformly distributed on the surface of nickel foam, and Ni₂P with abundant holes and saw-toothed morphology increase the

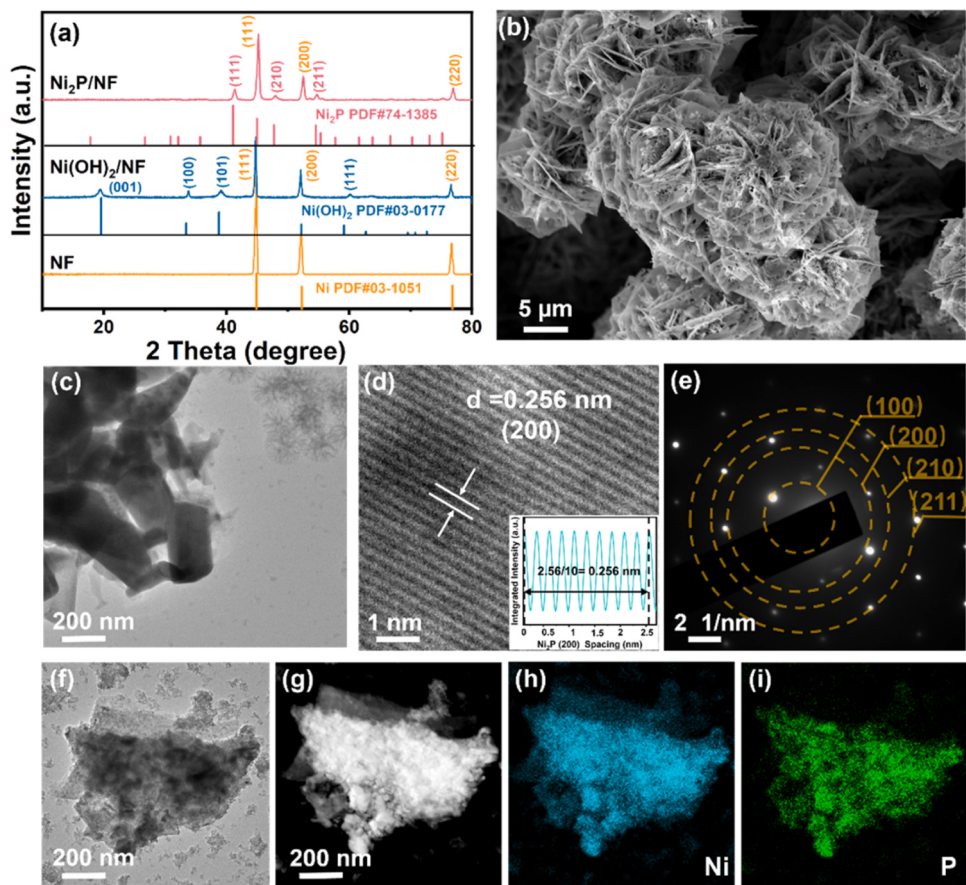


Fig. 1. The morphology and characterization of $\text{Ni}_2\text{P}/\text{NF}$ catalyst. (a) XRD patterns; (b) SEM; (c) TEM, (d) HRTEM, and (e) corresponding SAED pattern; (f and g) STEM image and corresponding element images of (h) Ni, (i) P.

surface area, which is beneficial for improving the catalytic activity (Fig. S1). The lattice fringe of 0.256 nm is assigned to (200) plane of Ni_2P (Fig. 1d) [41]. The selected area electron diffraction (SAED) pattern with diffraction rings are indexed to corresponding planes of Ni_2P (Fig. 1e). The elemental mapping images of a Ni_2P nano-unit reveal that the uniform distribution of Ni and P elements over the entire sample (Fig. 1f-i). All of the above results demonstrate the successful synthesis of Ni_2P .

The electrocatalytic FF oxidation performances of the samples are evaluated by linear sweep voltammogram (LSV) tests under the three-electrode system. As shown in Fig. 2a, $\text{Ni}_2\text{P}/\text{NF}$ exhibits more excellent catalytic activity for both OER and FOR than $\text{Ni}(\text{OH})_2/\text{NF}$. Compared with that of OER, the polarization curve of the $\text{Ni}_2\text{P}/\text{NF}$ for FOR exhibits obviously lower onset potential and increased current at the same overpotential. The $\text{Ni}_2\text{P}/\text{NF}$ can reach the current density of 100 mA cm^{-2} at $1.38 \text{ V}_{\text{RHE}}$ during the FOR, which is lower 230 mV than that of OER. It is demonstrated that the FOR over $\text{Ni}_2\text{P}/\text{NF}$ is more thermodynamically favorable than that of OER, and is expected to achieve low energy consumption for generating H_2 as well as the production of value-added chemical FA. In terms of Tafel slope in Fig. 2b, $\text{Ni}_2\text{P}/\text{NF}$ catalyst possess accelerating kinetics with 44 mV dec^{-1} , much lower than that of $\text{Ni}(\text{OH})_2/\text{NF}$ (86 mV dec^{-1}). Moreover, the highest ECSA (102.3 cm^2 in Table S1 of supporting information) of $\text{Ni}_2\text{P}/\text{NF}$ is obtained from the largest C_{dl} value of 3.58 mF cm^{-2} (Fig. S2), which might result from its hierarchical nanoflower-like morphology (Fig. 1b and c) with more exposed available active sites. In addition, the catalytic kinetics of catalysts has been evaluated by electrochemical impedance spectroscopy (EIS). Fig. S3 shows that the ohmic resistance (R_{s}) of catalysts is similar, resulting from the similar synthesis method. Compared with $\text{Ni}(\text{OH})_2/\text{NF}$, $\text{Ni}_2\text{P}/\text{NF}$ bears a much smaller charge-transfer

resistance (R_{ct}), indicating decent interfacial contact and rapid charge transfer between electrode and electrolyte. Fig. S4 indicates that $\text{Ni}_2\text{P}/\text{NF}$ electrode has excellent stability upon long-term tests (10 h at $1.60 \text{ V}_{\text{RHE}}$).

The FA production from electrocatalytic FOR has been proved via nuclear magnetic resonance (NMR), high performance liquid chromatography (HPLC), and Pyridine infrared (IR) spectroscopy (Figs. S5-S8). In this work, the FA produced from Cannizzaro reaction has been considered and calculated. Namely, FA production from both electrocatalytic oxidation and Cannizzaro reaction is denoted as general oxidation, while the real electro-oxidation represents FA generation only from electrocatalytic FOR. The stoichiometric quantities FAL was not detected by HPLC, mainly due to the high detection limit of FAL under operating condition (Fig. S9). The FOR performance (involving the yield, production rate, and faradaic efficiency (FE) of FA) of the catalysts were studied at different potentials from 1.40 to $1.60 \text{ V}_{\text{RHE}}$ in 1.0 M KOH anolyte with 50 mM FF (Fig. 2c-e and Fig. S10). Both of the yield and oxidation production are calculated via chronoamperometry test after FOR process for 30 min. Thereinto, the FA yield of $\text{Ni}_2\text{P}/\text{NF}$ shows 4–6 times higher than that of $\text{Ni}(\text{OH})_2/\text{NF}$, significantly observed from Fig. 2c and Fig. S11. Interestingly, the production rate of FA increases with applied potential, and $\text{Ni}_2\text{P}/\text{NF}$ performs the maximum production rate (Fig. 2d). Besides, more than 95 % FE for FA is achieved from general oxidation within the applied potential range. Even if FA from Cannizzaro reaction pathway is considered, there are still $\sim 85 \%$ FE for real electro-oxidation of FF to FA (Fig. 2e and Fig. S10). Furthermore, six-repeated FOR is conducted over $\text{Ni}_2\text{P}/\text{NF}$, with each cycle having at least 90 % FE for FA production, indicating that $\text{Ni}_2\text{P}/\text{NF}$ has high stability and selectivity during FOR (Fig. 2f).

HER under alkaline medium is one of the major route for industrial

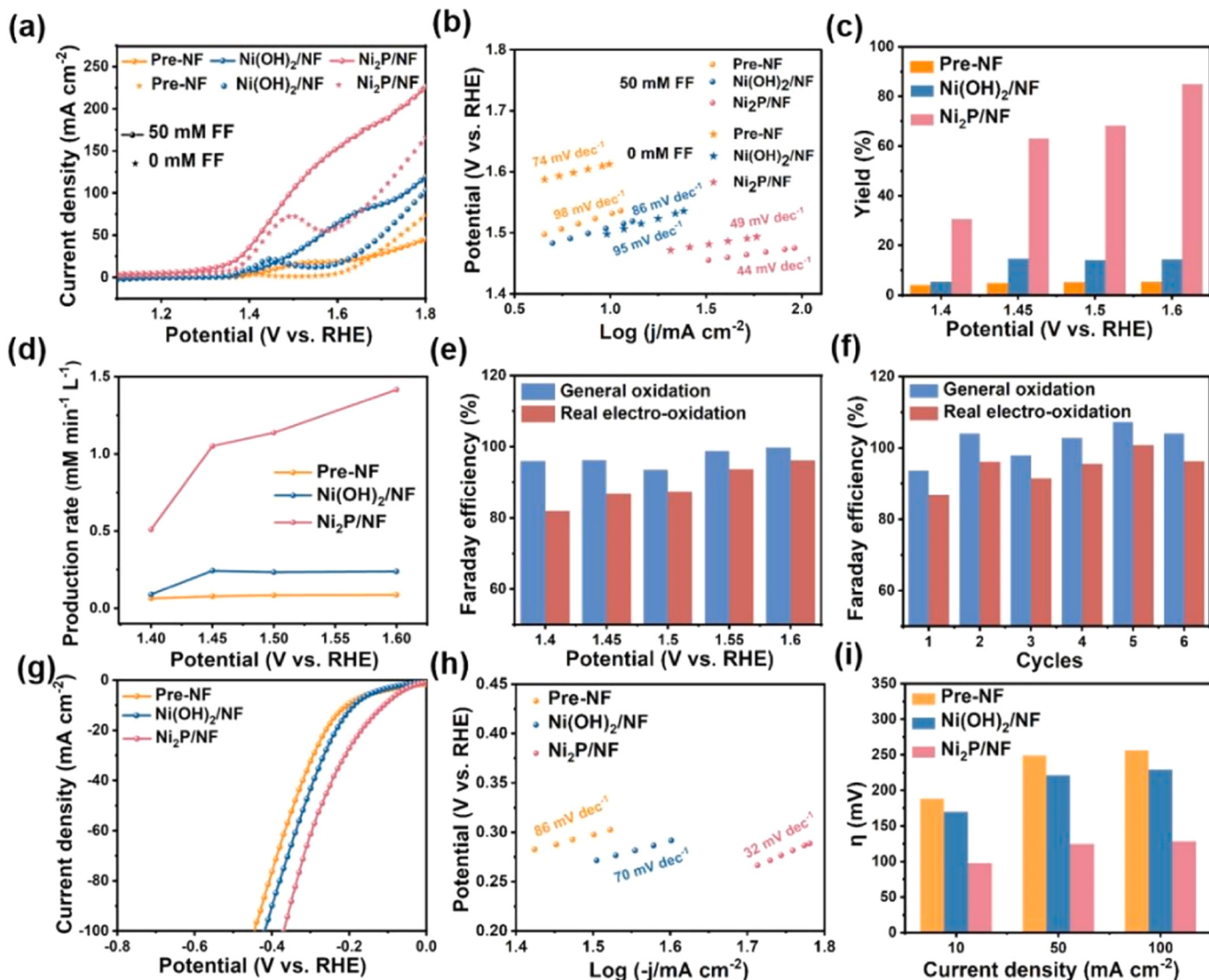


Fig. 2. FOR and HER performance in a three-electrode system. (a) LSV curves of three catalysts at a rate of 5 mV s^{-1} in 1.0 M KOH with and without 50 mM FF , and (b) the corresponding Tafel slopes; (c) Yield, and (d) Production rate of FA after 30 min FOR process; (e) FE of FF general oxidation and real electro-oxidation over $\text{Ni}_2\text{P}/\text{NF}$ catalyst at $50 \text{ }^\circ\text{C}$; (f) Cycles of FOR at 1.60 V ; (g) LSV curves of HER at a rate of 5 mV s^{-1} in 1.0 M KOH , (h) corresponding overpotentials at different current density, and (i) the corresponding Tafel slopes.

H_2 generation [42]. HER performances of as-synthesized catalysts are further explored. $\text{Ni}_2\text{P}/\text{NF}$ catalyst reaches the current density of 10 mA cm^{-2} at a much lower overpotential (98 mV) than $\text{Ni}(\text{OH})_2/\text{NF}$ (170 mV , Fig. 2g-i). $\text{Ni}_2\text{P}/\text{NF}$ exhibits a rather lower Tafel slope of 32 mV dec^{-1} than $\text{Ni}(\text{OH})_2/\text{NF}$ (70 mV dec^{-1}) for HER, indicating that $\text{Ni}_2\text{P}/\text{NF}$ owned a faster reaction kinetics. Benefiting from both the excellent HER and FOR performance of $\text{Ni}_2\text{P}/\text{NF}$, a two-electrode system with $\text{Ni}_2\text{P}/\text{NF}$ as cathode and anode was assembled. The current density of the whole system (HER || FOR) reaches $10/50 \text{ mA cm}^{-2}$ at $1.40/1.55 \text{ V}$, which is lower $133/223 \text{ mV}$ than that of overall water splitting (Fig. S12).

Based on the excellent FOR performance of Ni_2P , the evolution process of active phases and reaction pathways it undergoes during the electro-oxidation have been further investigated and explored. It is evident that *ex-situ* XRD shows that Ni_2P maintains its original phase structure during both OER and FOR in the range of $1.20\text{--}1.30 \text{ V}_{\text{RHE}}$ (Fig. 3a and b). Besides, the XPS spectra of Ni 2p after undergoing the OER process are slightly shifted, while no shift is seen in the NOR process. The shifted can be attributed to the presence of $\text{Ni}^{2+\delta}$ in $\text{Ni}_2\text{P}-\text{Ni}(\text{OH})_2$ after OER, resulting in an increase of Ni binding energy. After

NOR, Ni 2p there was no change in the Ni 2p peak implying that $\text{Ni}^{2+\delta}$ is not produced in $\text{Ni}_2\text{P}-\text{Ni}(\text{OH})_2$. This results of Ni 2p core level from XPS further demonstrates high-valence Ni species formation after OER, while the catalyst still remains the low-valence Ni species after FOR at $1.50 \text{ V}_{\text{RHE}}$ (Fig. 3c). As shown in Fig. S13, in the P 2p spectrum, the peaks at 134.0 eV can be ascribed to P-O, and the peaks at 129.7 eV can be attributed to metal phosphide (M-P). It shows that M-P disappeared after experiencing FOR and OER, explaining that the surface of the catalyst was reconstructed. Combined with Ni 2p spectrum and *ex-situ* XRD, indicating $\text{Ni}(\text{OH})_2$ have formed. Besides, the position of P-O did not shift after FOR compared with fresh Ni_2P , but after OER the position shifted 0.3 eV to the high binding energy, indicating that surface phosphate species are partial oxidized in the OER process.

For OER, the catalyst exhibits the new diffraction peaks belonging to $\text{Ni}(\text{OH})_2$ at $1.40 \text{ V}_{\text{RHE}}$, and the diffraction peaks gradually becomes stronger as the applied potential increases. The difference is that Ni_2P did not show any changes in structure before $1.60 \text{ V}_{\text{RHE}}$ under FOR conditions, and a weak $\text{Ni}(\text{OH})_2$ peak appeared at $1.70\text{--}1.80 \text{ V}_{\text{RHE}}$, implying that the voltage is greater than $1.70 \text{ V}_{\text{RHE}}$, $\text{Ni}(\text{OH})_2$ species accumulates. *In-situ* Raman spectroscopy was carried out to further

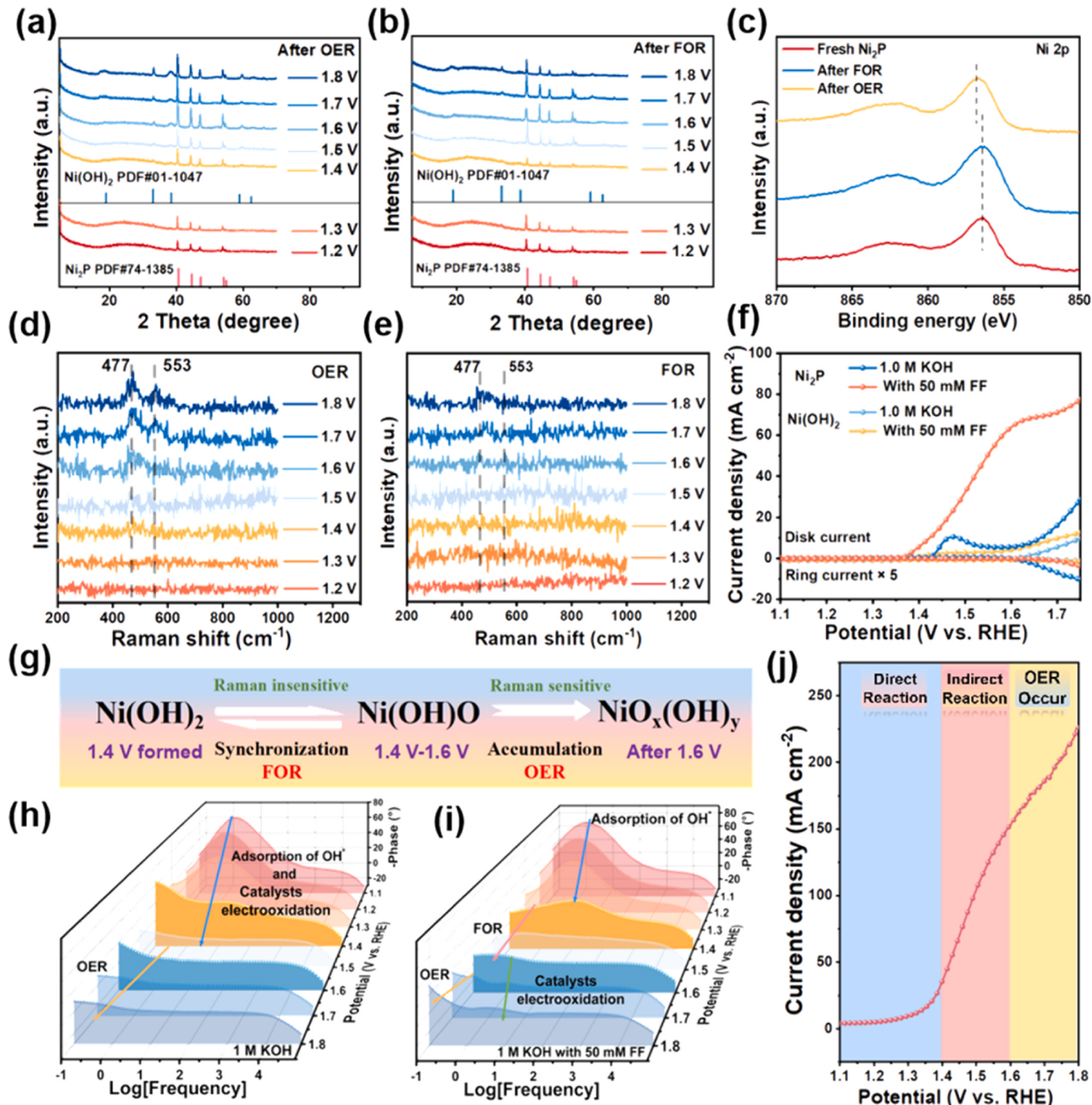


Fig. 3. The mechanism exploration of FOR over Ni₂P. (a and b) *Ex-situ* XRD results after OER and FOR at different applied potential; (c) XPS spectra for Ni 2p of Ni₂P after OER and FOR at 1.50 V_{RHE}; *In-situ* Raman spectra, (d) in 1.0 M KOH and (e) in 1.0 M KOH with 50 mM FF; (f) LSV curves of RRDE; (j) Evolution process of the surface Ni₂P; Bode plots of *in-situ* EIS over Ni₂P in (h) 1.0 M KOH and (i) in 1.0 M KOH with 50 mM FF; (j) LSV of FOR.

identify the structure evolution varied with the applied potential. In the Raman spectra, two peaks at 477 and 553 cm⁻¹ corresponded to Ni³⁺-O bending and stretching, respectively [43,44]. After 1.40 V_{RHE}, Ni³⁺-O of the oxide layer (Ni^{2+δ}O_xH_y) can be distinctly detected in the surface Ni₂P during OER process (Fig. 3d). Nevertheless, Ni³⁺-O species only accumulated after 1.70 V_{RHE} during FOR (Fig. 3e), which is in agreement with the results of XRD. No Ni³⁺-O vibration peaks observed from 1.40 to 1.60 V_{RHE} is due to the fact that the as-reconstructed surface Ni(OH)₂ during FOR process is ultrathin, which can be considered as a single layer of Ni(OH)₂ covered on Ni₂P (Ni₂P-Ni(OH)₂). The hydrogen

defect of Ni(OH)O can be filled by electrons and protons of excess FF promptly and completely (Ni₂P-Ni(OH)O + H_{FF} + e_{FF} = Ni₂P-Ni(OH)₂), so that the electronic structure of Ni₂P-Ni(OH)₂ can remain unchanged. This is accordance to the “Electro-chemical-Chemical” reaction pathway in the range of 1.40–1.60 V_{RHE} [7,37]. After 1.70 V_{RHE} in the FOR system, the electron transfer rate of the Ni₂P-Ni(OH)₂ catalyst dehydrogenation reaction (Ni₂P-Ni(OH)₂ + OH⁻ = Ni₂P-Ni(OH)O) is faster than that of the FF dehydrogenation reaction (Ni₂P-Ni(OH)O + H_{FF} + e_{FF} = Ni₂P-Ni(OH)₂), which lead to local phase transition and passivation (Fig. 3e).

In order to further distinguish the competition between FOR and OER on the Ni₂P surface, the measurements on rotating ring-disk electrode (RRDE) were carried out (Fig. 3f). It is found that no ring current in the polarization curves of Ni₂P during OER process from 1.10 to 1.60 V_{RHE}, in which the raised disk current is attributed to the catalysts oxidation (Ni₂P → Ni^{2+δ}O_xH_y). When 50 mM FF was added into the electrolyte, the disk current increased at 1.40 V_{RHE}, while there is no ring current response until 1.60 V_{RHE}. The results demonstrate that OER as an inevitable competing reaction of FOR, is well inhibited at

1.40–1.60 V_{RHE} on Ni₂P-Ni(OH)₂. According to the above results, the evolution process and reaction mechanism of Ni₂P as the active phase with the applied potential in FOR under 1.0 M KOH with 50 mM FF have been proposed in Fig. 3g. Specifically, at 1.30–1.40 V_{RHE}, Ni₂P serves as active phase directly electro-oxidized FF to FA by the surface adsorbed OH^{*}. Then the surface reconstruction of Ni₂P occurred and in-situ formed single-layer oxide heterostructure of Ni₂P-Ni(OH)₂ dramatically enhanced electro-oxidation of FF to FA via an indirect reaction pathway at 1.40–1.60 V_{RHE}. After exceeding 1.6 V_{RHE}, OER will occur

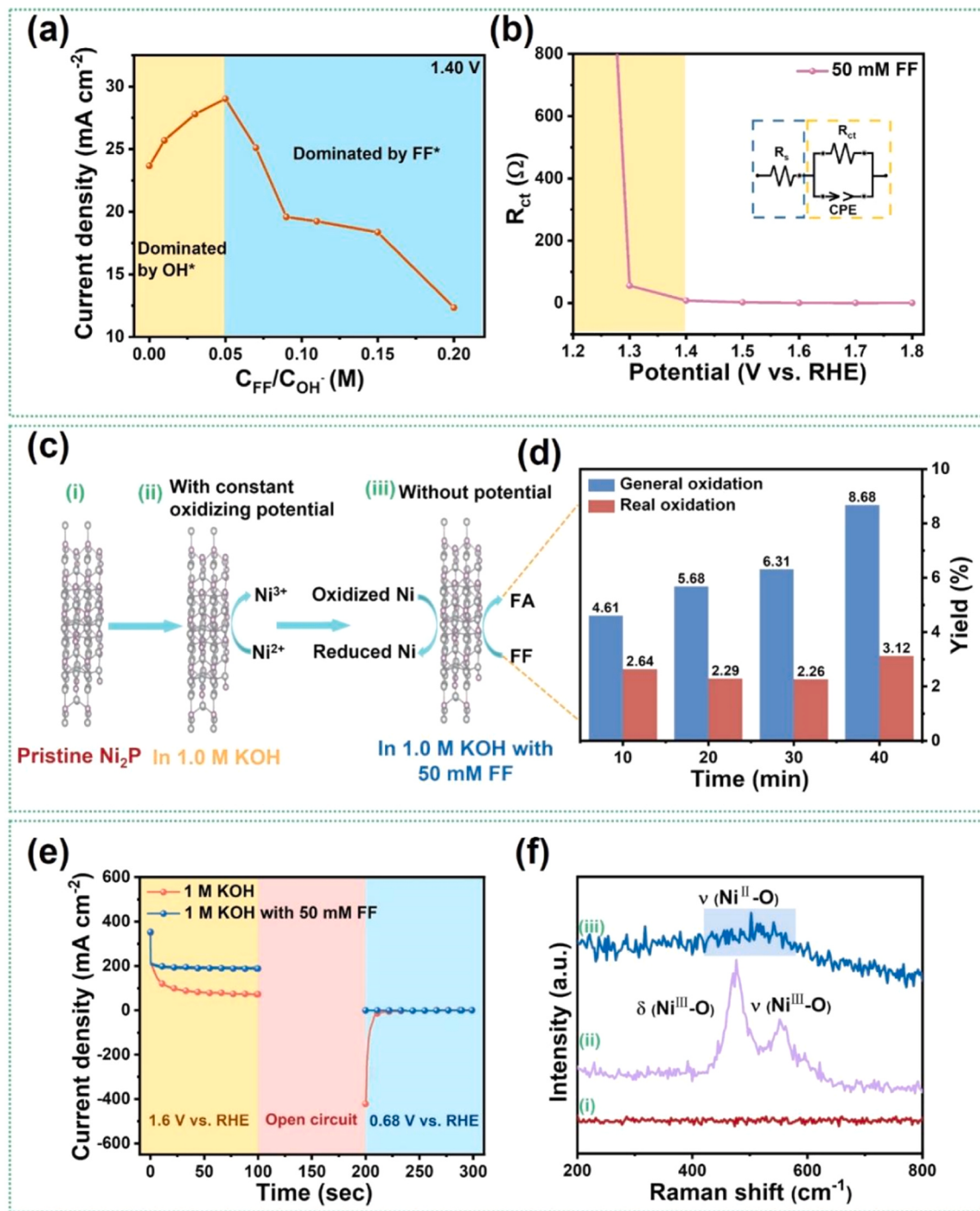


Fig. 4. The revelation of electrocatalytic reaction pathway of FOR. (a) The relationship between current density and $C_{\text{FF}}/C_{\text{OH}^-}$ at 1.40 V_{RHE}; (b) fitting resistance (R_{ct}) over Ni₂P electrode in 50 mM FF electrolyte and corresponding fitting model is shown as inset; (c) Three steps of designed experiments; (d) The yield of FF oxidation corresponding to the third step in (c); (e) The multi-potential step measurements of Ni₂P in 1.0 M KOH with and without 50 mM FF; (f) The corresponding Raman spectra of such three steps in (c).

with the Ni(OH)₂O accumulation and Ni(OH)₂ formation.

The in-situ EIS measurement was adopted to reveal the potential-dependent reaction interface during OER and FOR [45,46]. The kinetics of oxidation reaction and interfacial reaction of the sample are illustrated with the combination of Bode plot and Nyquist plot (Figs. 3h, 3i and S14). Generally, the high-frequency region (10–10⁵ Hz) is related to the process of electro-oxidation of OH⁻ to OH* (* + OH⁻ → OH* + e⁻, which is the active species for direct FF oxidation) on the Ni₂P surface and/or direct oxidation of electrode materials, namely the oxidation of Ni₂P is occurred. The low-frequency region (0.1–10 Hz) is connected with the OER process [7]. Based on the potential consistency between the LSV curve and in-situ EIS during OER at 1.10–1.60 V_{RHE}, there were two different interface reactions, including the adsorbed OH⁻ oxidized to OH* and catalyst electro-oxidation at 1.10–1.50 V_{RHE} occurring at the high-frequency interface and OER occurring at the low-frequency interface (Fig. 3h, and S15) [46]. For the FOR system at 1.40–1.60 V_{RHE}, new transition peaks took place with high current density, which proves that FOR occurs at the high-frequency interface on the Ni₂P-Ni(OH)₂ (Fig. 3i). The peaks in the low-frequency region indicate that OER and FOR simultaneously occurred after 1.70 V_{RHE}. Combining *ex situ* XRD, *in situ* Raman, and operando EIS, we found that the active phase of Ni₂P undergoes different evolution processes in the OER and FOR processes, and identified the origin of FOR activity.

Different C_{FF}/C_{OH-} ratios were used to investigate the competitive adsorption effect of FF and OH⁻ on FOR performance. Fig. 4a shows the volcano-type curve between the current density and C_{FF}/C_{OH-} at 1.40 V_{RHE}. Based on Stern's double-layer model, the adequate OH⁻ is easily adsorbed on the surface of Ni₂P and electro-oxidized to form adsorbed OH* (* + OH⁻ - e⁻ → OH*) [34]. Once the C_{FF}/C_{OH-} ratio is higher than 0.05, there is no enough OH* reacted with superfluous FF adsorbed on Ni₂P surface. Correspondingly, 50 mM FF has been selected for all electrochemical performance test and mechanistic study (Fig. 4a, S16 and S17). The relationship between R_{ct} (R_{ct}: the resistance of the interfacial charge transfer reaction) and oxidation potential reveals the reaction kinetics of oxidation (Fig. 4b and S18). After adding FF in the electrolyte, the R_{ct} at 1.00–1.20 V_{RHE} is huge, indicating weaker charge transfer between electrode and reaction interface [47]. With the applied potential increase (at 1.30–1.40 V_{RHE}) on Ni₂P, the value of R_{ct} further decreases, indicating FOR occurred on Ni₂P. The period at 1.20–1.40 V_{RHE} belongs to the direct oxidation of FF [48], because the applied potential is lower than the catalyst oxidation potential of 1.40 V_{RHE} (Fig. 3j and S16), suggesting that FF can be oxidized to FA without the participation of high-valence Ni species. While the potential is higher than 1.60 V_{RHE}, the value of R_{ct} is similar to that of OER (Fig. S18), and thus the OER occurred (Fig. 3j).

In order to investigate the mechanism of indirect oxidation reactions, pristine Ni₂P/NF was placed into 1.0 M KOH solution with 50 mM FF. After 30 min of electrode oxidation reaction at 1.60 V_{RHE}, the electrode was immediately transferred into 1.0 M KOH with 50 mM FF electrolyte without applied potential (Fig. 4c). The product FA was detected and quantified by HPLC, and ~2 % FA generation was from spontaneously chemical oxidation process after considering Cannizzaro reaction. Fig. 4d show that the amount of FA obtained by FF oxidation was similar after different times. Therefore, the in-situ formed single-layer oxide heterostructure of Ni₂P-Ni(OH)₂ follows the "Electro-chemical-Chemical" indirect oxidation pathway at 1.40–1.60 V_{RHE}, namely Ni₂P-Ni(OH)₂ O electrochemically produced from in-situ produced Ni₂P-Ni(OH)₂ by dehydrogenation and then oxidize FF molecule spontaneously. In addition, to further study the indirect oxidation reactions mechanism of the catalyst, the multi-potential step curves were investigated. Firstly, high potential was applied to generate high-valence Ni species (Ni(OH)₂O), and then it was switched to an open circuit potential (OCP). The response of reduction current without FF is assigned to the transformation of high-valence Ni to low-valence Ni species. While there is nearly no current response when 50 mM FF existed in the electrolyte, indicating that produced high-valence Ni species spontaneously

oxidized the FF to FA. Raman results in Fig. 4f manifest that the catalyst is transformed corresponding to the above processes in Fig. 4c. The produced high-valence Ni³⁺ (477 and 553 cm⁻¹) under chronoamperometry test in step 2 converts to reduced Ni²⁺ species during FF oxidation in step 3. These results further demonstrate the structural evolution and reveal the catalytic mechanism of Ni₂P in the whole process of electro-catalytic oxidation.

The adsorption of reactant FF plays a vital role in FF oxidation process, we combined OCP measurement with fourier transform infrared spectroscopy (FT-IR) to evaluate FF adsorption over these catalysts [49]. Fig. 5a reveals that after injecting 50 mM FF into 1.0 M KOH electrolyte, a decrease of OCP of electrochemical cell over different electrodes can be observed. Compared with 0.02 V decrease for Ni(OH)₂/NF, a more significant OCP decrease for Ni₂P/NF (0.16 V) and Ni₂P-Ni(OH)₂/NF (0.16 V, the Ni₂P-Ni(OH)₂/NF catalyst was obtained via FOR of Ni₂P/NF at 1.60 V_{RHE} for 30 min) suggests a stronger adsorption of FF in the presence of Ni₂P constituent. Besides, FT-IR spectroscopy was performed over Ni₂P, Ni(OH)₂ and Ni₂P-Ni(OH)₂ catalysts. As shown in Fig. 5b, FF was evidently absorbed on catalysts (in Fig. S19, for the pure FF, the peak of C=O stretching vibration in the aldehyde group appears around 1730 cm⁻¹. And When FF is adhere to the catalyst, the C=O stretching vibration can be seen in the catalysts, indicating that FF is adsorbed on the catalysts, in Figs. S20). Fig. 5b shows that the band centered at ~1700 cm⁻¹ is attributed to ν_{C=O} and the peaks at 1390–1570 cm⁻¹ belongs to ν_{C=C} of furan ring of FF. Compared with ν_{C=O} at 1763 cm⁻¹ over pure Ni(OH)₂, an evident redshift of ν_{C=O} in FF can be observed over Ni₂P/NF and Ni₂P-Ni(OH)₂/NF, indicating that Ni₂P-based constituent shows stronger chemical adsorption of FF than Ni(OH)₂. Thereinto, the redshift of ca. 45 cm⁻¹ suggests the elongation and weakening of C=O bond, which facilitates C=O cleavage and further dehydrogenation [50]. Furthermore, the heterostructure of Ni₂P-Ni(OH)₂/NF was further demonstrated by the FT-IR spectrum, seeing from the stretching vibration of O-H (ν_{O-H}) and Ni-O band (ν_{Ni-O}) of Ni(OH)₂ in Fig. S21.

In view of reactive electrophilic oxygen species from catalyst dehydrogenation is currently regarded as key step of NOR [7], DFT calculation was applied to further evaluate the dehydrogenation capacity of these catalysts. The differential charge density plot in Fig. 5c shows the electrons transfer from Ni(OH)₂ to Ni₂P at the interface of Ni₂P-Ni(OH)₂, leading to electrophilic and nucleophilic region generation at the interface of Ni₂P-Ni(OH)₂, which is beneficial to FF adsorption and subsequent oxidation reaction. To the best of our knowledge, the dehydrogenation ability of electrocatalyst is very important for the FOR activity. As shown in Fig. 5d, Ni₂P-Ni(OH)₂ has the lowest Gibbs free energy of 0.29 eV rather than that of Ni₂P (0.47 eV) and Ni(OH)₂ (0.98 eV), suggesting that Ni₂P-Ni(OH)₂ is inclined to form Ni₂P-Ni(OH)₂ O with lower generation potential and superior FOR performance.

Besides, FF oxidation reaction pathway has been deduced to deeply understand the reaction mechanism. For the spontaneous Cannizzaro reaction which we have excluded during the real FOR, OH⁻ directly attacked to aldehyde group of FF and thus FF is oxidized to furoate in the alkaline medium (Fig. S22) [51]. More importantly, geminal diol is rapidly formed via FF hydration for the first step of FOR in alkaline condition (Fig. 5e) [52]. Next, the deprotonation of geminal diol reaction occurred, in which OH⁻ seized H of a hydroxyl group in geminal diols to attain Gem-diolate anions (GDA). Finally, FA is formed via proton coupled electron transfer (PCET) process, which can be considered as a rate-determining step (RDS) for FF oxidation.

We have particularly explored and revealed the structure evolution and corresponding reaction pathways over Ni₂P in the whole applied potential during electrocatalytic FOR. Inspired by the enhancement of FOR performance via heterostructure of Ni₂P-Ni(OH)₂ formed by in-situ surface reconstruction, we have further tested and verified other nickel-based X-ide (NiX-ide). As shown in Figs. 6a and 6b, the polarization curve of the Ni₂P for FOR and OER exhibits obviously lower onset potential and increased current at the same overpotential compared with

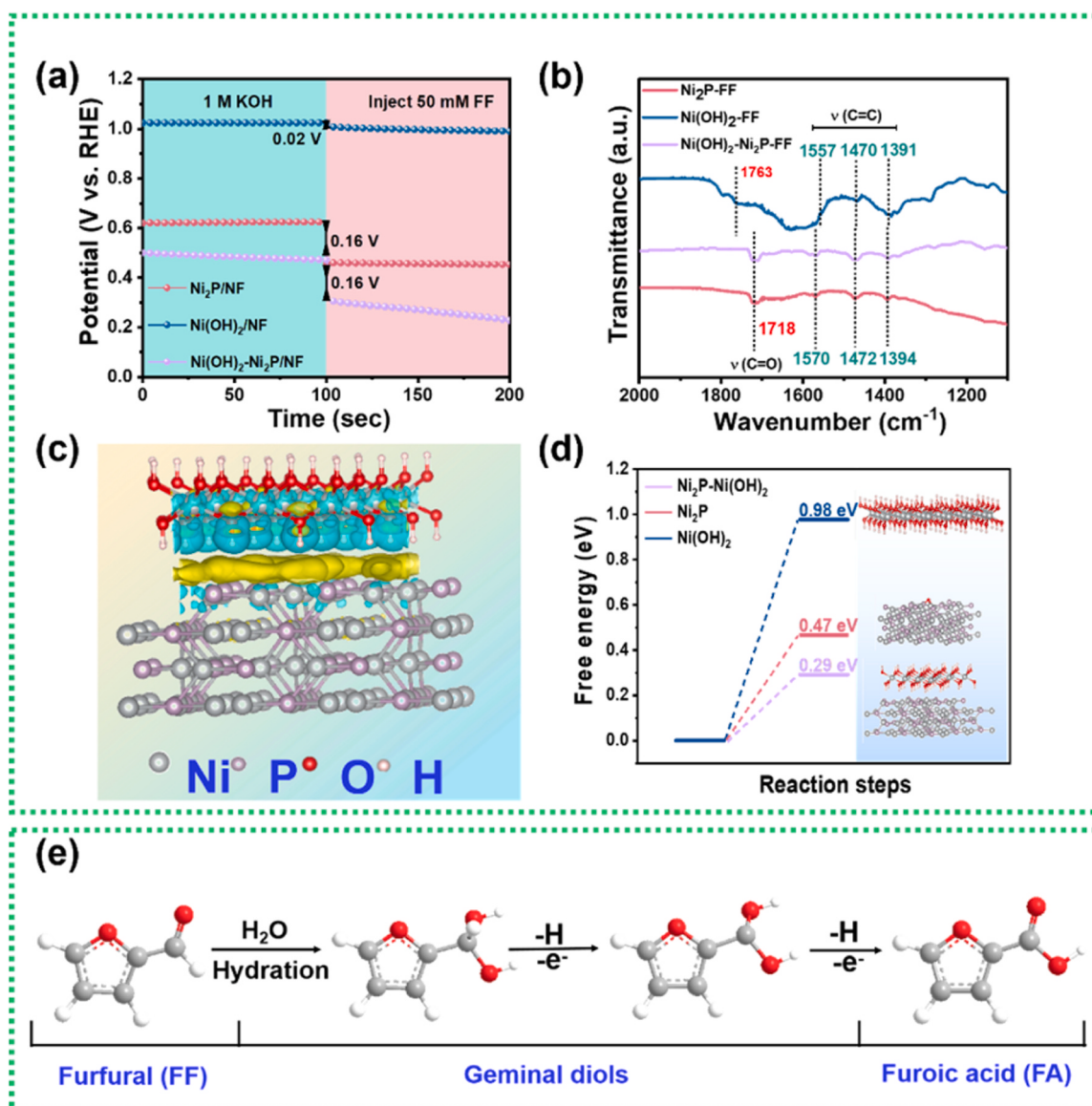


Fig. 5. The (a) OCP curves of Ni₂P/NF, Ni(OH)₂/NF, and Ni₂P-Ni(OH)₂/NF in 1.0 M KOH with subsequent injection of 50 mM FF; (b) FT-IR of FF adsorption over different catalysts; (c) Differential charge density plot of Ni₂P-Ni(OH)₂; (d) Free energy diagram for the dehydrogenation reaction of Ni₂P, Ni(OH)₂, and Ni(OH)₂-Ni₂P and their corresponding DFT-optimized configurations; (e) Proposed reaction pathway of FF electrocatalytic oxidation.

the other X-side catalysts. This suggests that it is easier to form heterojunctions Ni₂P-Ni(OH)₂ than that of other catalysts. In addition, as shown in Fig. S23, the results of DFT calculations show that Ni₂P-Ni(OH)₂ has the lowest Gibbs free energy of 0.29 eV, lower than that of Ni₂S-Ni(OH)₂ (0.47 eV) and Ni₂Se-Ni(OH)₂ (0.98 eV), meaning that Ni₂P-Ni(OH)₂ has the best catalytic performances. The theoretical calculation results are consistent with the experimental phenomenon. Besides, we further adopted Ni₂P and Ni(OH)₂ catalysts for catalytic oxidation of some representative substrates with aldehyde group. Remarkably, lower onset potential (~1.35 V_{RHE}) and higher current density of aldehyde oxidation demonstrates that Ni₂P is more favorable for such selected substrates oxidation than Ni(OH)₂ owing to the in-situ formed Ni₂P-Ni(OH)₂ heterostructure from surface reconstruction with the potential-dependent electrocatalytic behavior (Fig. 6b-f).

4. Conclusion

In summary, Ni₂P and FF are selected as the model catalyst and nucleophile to investigate the structure evolution and corresponding

reaction mechanism over NiX-ide in the whole applied potential during electrocatalytic FOR. With *ex-situ* and *in-situ* characterization study and electrochemical test, a three-step evolution process would occur over Ni₂P and strongly depends on the applied potential during the FOR. Ni₂P act as active phase directly oxidized FF to FA with a relatively weak activity at 1.30–1.40 V_{RHE}. Then the surface reconstruction of Ni₂P initiated at 1.40–1.60 V_{RHE}, and *in-situ* constructed single oxide layer of Ni₂P-Ni(OH)₂ heterostructure remarkably enabling high-performance of FOR in an indirect way. 95 % FA selectivity and 85 % faradaic efficiency (FE) after deducting FF Cannizzaro reaction were obtained under alkaline condition. OER inevitably competes with FOR after exceeding 1.60 V_{RHE}, accompanied by the accumulation of Ni(OH)₂. The experimental and theoretical results reveal that the *in situ* formed Ni₂P-Ni(OH)₂ heterostructure shows strong FF adsorption and bears low dehydrogenation energy, which promotes the RDS of FOR and gives excellent FOR performance. Besides, the proposed dynamic heterostructure model of Ni₂P-Ni(OH)₂ derived from Ni₂P has been validated for its universality to other X-ides (NiS and NiSe₂) for FOR and other nucleophilic reagents. This work not only sheds light on the mechanistic exploration

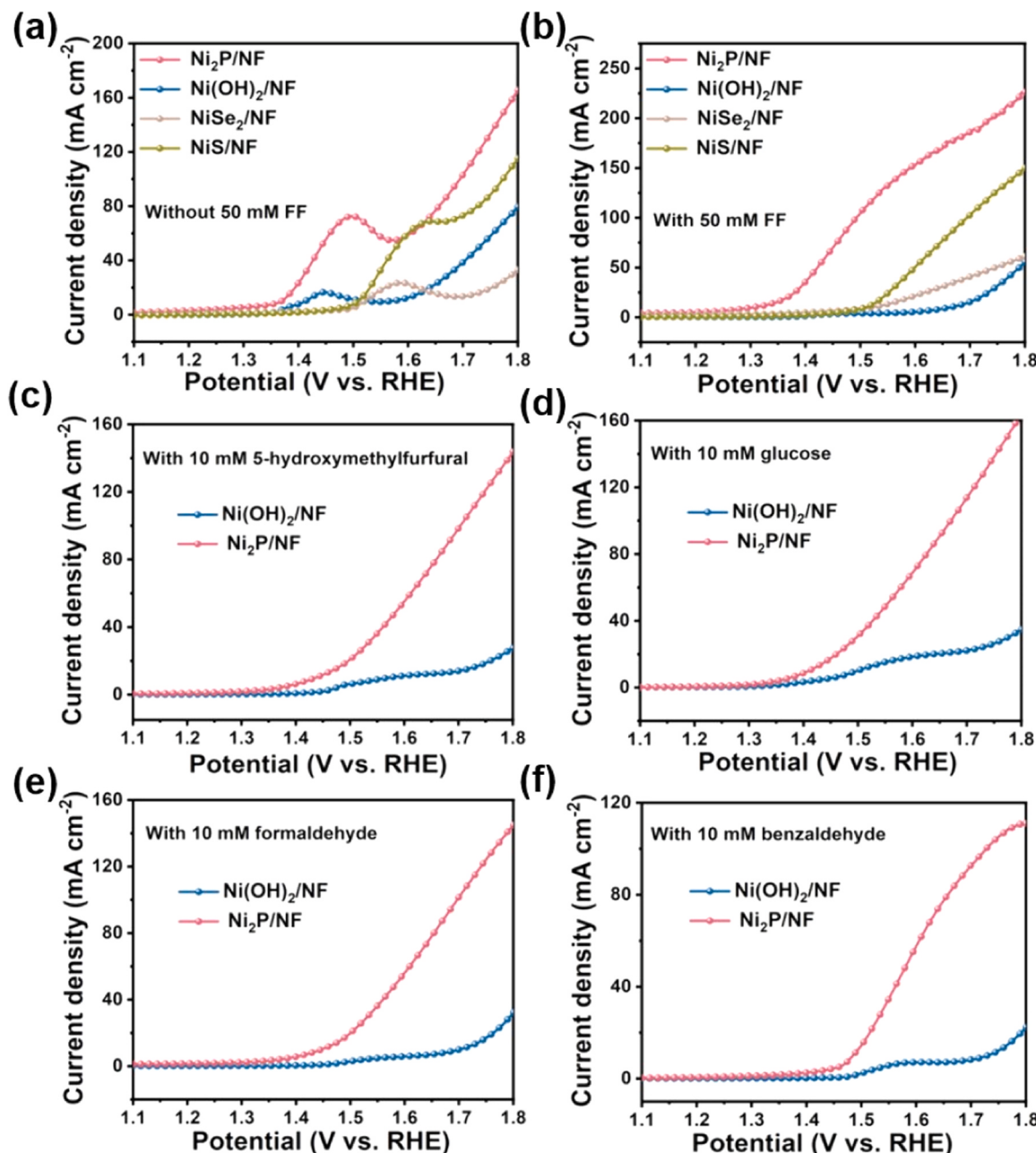


Fig. 6. LSV curves for different catalyst in (a) 1.0 M KOH, and (b) 1.0 M KOH with 50 mM FF LSV curves for Ni₂P/NF and Ni(OH)₂/NF in 1.0 M KOH with 10 mM (c) HMF, (d) glucose, (e) formaldehyde, and (f) benzaldehyde.

and insights of nickel-based X-ide for electro-oxidation reaction, but also provide the guidance for the development of nucleophile oxidation reaction and organic electrosynthesis.

CRediT authorship contribution statement

Zhikun Peng: Conceptualization, Investigation, Methodology, Funding acquisition, Resources, writing – review and editing. **Siying Li:** Methodology, methodology, validation. **Rui Li:** Methodology, methodology, data curation; formal analysis, writing – original draft. **Kaihang Sun:** software, supervision. **Jianpeng Li:** validation, writing – review and editing. **Yanyan Liu:** resources. **Zhongyi Liu:** resources. **Yongjing Wang:** software, visualization. **Jingmin Ge:** conceptualization; data curation; formal analysis, writing – review and editing. **Kun Xiang:** supervision, validation, project administration, writing – review and editing.

Declaration of Competing Interest

The authors declare that they have no known competing financial interests or personal relationships that could have appeared to influence the work reported in this paper.

Data availability

No data was used for the research described in the article.

Acknowledgements

This work was supported by National Natural Science Foundation of China (No. 22278380), China Postdoctoral Science Foundation (2021M692911, 2022T150589). The Knowledge Innovation Program of Wuhan Shuguang Project (2022010801020355). This work is supported

by National Supercomputing Center in Zhengzhou.

Appendix A. Supporting information

Supplementary data associated with this article can be found in the online version at doi:10.1016/j.apcatb.2023.123450.

References

- [1] S. Huang, B. Gong, Y. Jin, P.H.L. Sit, J.C. Lam, The structural phase effect of MoS₂ in controlling the reaction selectivity between electrocatalytic hydrogenation and dimerization of furfural, *ACS Catal.* 12 (2022) 11340–11354.
- [2] A. Corma, S. Iborra, A. Velty, Chemical routes for the transformation of biomass into chemicals, *Chem. Rev.* 107 (2007) 2411–2502.
- [3] C. Xu, E. Paone, D. Rodriguez-Padron, R. Luque, F. Mauriello, Recent catalytic routes for the preparation and the upgrading of biomass derived furfural and 5-hydroxymethylfurfural, *Chem. Soc. Rev.* 49 (2020) 4273–4306.
- [4] J.Q. Bond, D.M. Alonso, D. Wang, R.M. West, J.A. Dumesic, Integrated catalytic conversion of Gamma-valerolactone to liquid alkenes for transportation fuels, *Science* 327 (2010) 1110–1114.
- [5] W. Xu, C. Yu, J. Chen, Z. Liu, Electrochemical hydrogenation of biomass-based furfural in aqueous media by Cu catalyst supported on N-doped hierarchically porous carbon, *Appl. Catal. B: Environ.* 305 (2022), 121062.
- [6] J. Wang, X. Dai, H. Wang, H. Liu, J. Rabeha, A. Brickner, F. Shi, M. Gong, X. Yang, Dihydroxyacetone valorization with high atom efficiency via controlling radical oxidation pathways over natural mineral-inspired catalyst, *Nat. Commun.* 12 (2021) 6840.
- [7] W. Chen, C. Xie, Y. Wang, Y. Zou, C. Dong, Y. Huang, Z. Xiao, Z. Wei, S. Du, C. Chen, B. Zhou, J. Ma, S. Wang, Activity origins and design principles of Nickel-based catalysts for nucleophile electrooxidation, *Chem* 6 (2020) 2974–2993.
- [8] K. Xiang, D. Wu, X. Deng, M. Li, S. Chen, P. Hao, X. Guo, J.L. Luo, X.Z. Fu, Boosting H₂ generation coupled with selective oxidation of methanol into value-added chemical over cobalt hydroxide@hydroxysulfide nanosheets electrocatalysts, *Adv. Funct. Mater.* 30 (2020) 1909610.
- [9] K. Xiang, Z. Song, D. Wu, X. Deng, X. Wang, W. You, Z. Peng, L. Wang, J.L. Luo, X. Z. Fu, Bifunctional Pt-Co₃O₄ electrocatalysts for simultaneous generation of hydrogen and formate via energy-saving alkaline seawater/methanol co-electrolysis, *J. Mater. Chem. A* 9 (2021) 6316–6324.
- [10] R. Li, K. Xiang, Z. Peng, Y. Zou, S. Wang, Recent advances on electrolysis for simultaneous generation of valuable chemicals at both anode and cathode, *Adv. Energy Mater.* 11 (2021) 2102292.
- [11] B. Zhao, C. Xu, M. Shakouri, R. Feng, Y. Zhang, J. Liu, L. Wang, J. Zhang, J.L. Luo, X.Z. Fu, Anode-cathode interchangeable strategy for in situ reviving electrocatalysts' critical active sites for highly stable methanol upgrading and hydrogen evolution reactions, *Appl. Catal. B: Environ.* 305 (2022), 121082.
- [12] D. Li, Z. Li, R. Zou, G. Shi, Y. Huang, W. Yang, W. Yang, C. Liu, X. Peng, Coupling overall water splitting and biomass oxidation via Fe-doped Ni₂P@C nanosheets at large current density, *Appl. Catal. B: Environ.* 307 (2022), 121170.
- [13] Y. Sun, H. Shin, F. Wang, B. Tian, C. Chiang, S. Liu, X. Li, Y. Wang, L. Tang, W. A. Goddard, M. Ding, Highly selective electrocatalytic oxidation of amines to nitriles assisted by water oxidation on metal-doped α -Ni(OH)₂, *J. Am. Chem. Soc.* 144 (2022) 15185–15192.
- [14] Y. Kwon, K.J.P. Schouten, J.C. van der Waal, E. de Jong, M.T.M. Koper, Electrocatalytic conversion of furanic compounds, *ACS Catal.* 6 (2016) 6704–6717.
- [15] M. Douthwaite, X. Huang, S. Iqbal, P.J. Miedzak, G.L. Brett, S.A. Kondrat, J. K. Edwards, M. Sankar, D.W. Knight, D. Bethell, G.J. Hutchings, The controlled catalytic oxidation of furfural to furoic acid using AuPd/Mg(OH)₂, *Catal. Sci. Technol.* 7 (2017) 5284–5293.
- [16] C.D. Hurd, J.W. Garrett, E.N. Osborne, Furan reactions. IV. furoic acid from furfural, *J. Am. Chem. Soc.* 55 (1933) 1082–1084.
- [17] X. Huang, Y. Liu, H. Wen, R. Shen, S. Mehdi, X. Wu, E. Liang, X. Guo, B. Li, Ensemble-boosting effect of Ru-Cu alloy on catalytic activity towards hydrogen evolution in ammonia borane hydrolysis, *Appl. Catal. B: Environ.* 287 (2021), 119960.
- [18] Z. Zhou, Y. Xie, L. Sun, Z. Wang, W. Wang, L. Jiang, X. Tao, L. Li, X. Li, G. Zhao, Strain-induced in situ formation of NiOOH species on Co-Co bond for selective electrooxidation of 5-hydroxymethylfurfural and efficient hydrogen production, *Appl. Catal. B: Environ.* 305 (2022), 121072.
- [19] Y. Song, W. Xie, Y. Song, H. Li, S. Li, S. Jiang, J.Y. Lee, M. Shao, Bifunctional integrated electrode for high-efficient hydrogen production coupled with 5-hydroxymethylfurfural oxidation, *Appl. Catal. B: Environ.* 312 (2022), 121400.
- [20] N. Jiang, X. Liu, J. Dong, B. You, X. Liu, Y. Sun, Electrocatalysis of furfural oxidation coupled with H₂ evolution via Nickel-based electrocatalysts in water, *ChemNanoMat* 3 (2017) 491–495.
- [21] B. You, X. Liu, N. Jiang, Y. Sun, A general strategy for decoupled hydrogen production from water splitting by integrating oxidative biomass valorization, *J. Am. Chem. Soc.* 138 (2016) 13639–13646.
- [22] B. Garlyyev, S. Xue, J. Fichtner, A.S. Bandarenka, C. Andronescu, Prospects of Value-added chemicals and hydrogen via electrolysis, *ChemSusChem* 13 (2020) 2513–2521.
- [23] G. Chamoulaud, D. Floner, C. Moinet, C. Lamy, E.M. Belgsir, Biomass conversion II: simultaneous electrosyntheses of furoic acid and furfuryl alcohol on modified graphite felt electrodes, *Electrochim. Acta* 46 (2001) 2757–2760.
- [24] X. Zhang, M. Han, G. Liu, G. Wang, Y. Zhang, H. Zhang, H. Zhao, Simultaneously High-rate furfural hydrogenation and oxidation upgrading on nanostructured transition metal phosphides through electrocatalytic conversion at ambient conditions, *Appl. Catal. B: Environ.* 244 (2019) 899–908.
- [25] G. Bharath, F. Banat, High-Grade biofuel synthesis from paired electrohydrogenation and electrooxidation of furfural using symmetric Ru/reduced graphene oxide electrodes, *ACS Appl. Mater. Interfaces* 13 (2021) 24643–24653.
- [26] H. Liu, W. Li, Recent advances in paired electrolysis of biomass-derived compounds toward cogeneration of value-added chemicals and fuels, *Curr. Opin. Electrochem.* 30 (2021), 100795.
- [27] S. Barwe, J. Weidner, S. Cychy, D.M. Morales, S. Dieckhöfer, D. Hiltrop, J. Masa, M. Muhler, W. Schuhmann, Electrocatalytic oxidation of 5-(Hydroxymethyl)furfural using High-surface-area nickel boride, *Angew. Chem. Int. Ed.* 57 (2018) 11460–11464.
- [28] X. Guan, Q. Wu, H. Li, S. Zeng, Q. Yao, R. Li, H. Chen, Y. Zheng, K. Qu, Identifying the roles of Ru single atoms and nanoclusters for energy-efficient hydrogen production assisted by electrocatalytic hydrazine oxidation, *Appl. Catal. B: Environ.* 323 (2023), 122145.
- [29] Y. Xu, M. Liu, M. Wang, T. Ren, K. Ren, Z. Wang, X. Li, L. Wang, H. Wang, Methanol electroreforming coupled to green hydrogen production over bifunctional NiIr-based metal-organic framework nanosheet arrays, *Appl. Catal. B: Environ.* 300 (2022), 120753.
- [30] H. Zhong, Q. Zhang, J. Yu, X. Zhang, C. Wu, Y. Ma, H. An, H. Wang, J. Zhang, X. Wang, J. Xue, Fundamental understanding of structural reconstruction behaviors in oxygen evolution reaction electrocatalysts, *Adv. Energy Mater.* (2023), 2301391.
- [31] Z. Ji, W. Yuan, S. Zhao, Local supermetastable active structure via electrochemical reconstruction toward electrooxidation process, *Chem. Catal.* 3 (2023), 100501.
- [32] W. Zhang, Y. Yang, Y. Tang, Q. Gao, In-situ reconstruction of catalysts in cathodic electrocatalysis: New insights into Active-site structures and working mechanisms, *J. Energy Chem.* 70 (2022) 414–436.
- [33] B. You, N. Jiang, X. Liu, Y. Sun, Simultaneous H₂ generation and biomass upgrading in water by an efficient Noble-metal-free bifunctional electrocatalyst, *Angew. Chem. Int. Ed.* 55 (2016) 9913–9917.
- [34] R. Luo, Y. Li, L. Xing, N. Wang, R. Zhong, Z. Qian, C. Du, G. Yin, Y. Wang, L. Du, A dynamic Ni(OH)₂-NiOOH/NiFeP heterojunction enabling high-performance E-upgrading of hydroxymethylfurfural, *Appl. Catal. B: Environ.* 311 (2022), 121357.
- [35] S.R. Kubota, K. Choi, Electrochemical valorization of furfural to maleic acid, *ACS Sustain. Chem. Eng.* 6 (2018) 9596–9600.
- [36] C. Chen, L. Wang, B. Zhu, Z. Zhou, S.I. El-Hout, J. Yang, J. Zhang, 2,5-Furandicarboxylic acid production via catalytic oxidation of 5-hydroxymethylfurfural: catalysts, processes and reaction mechanism, *J. Energy Chem.* 54 (2021) 528–554.
- [37] W. Chen, Y. Wang, B. Wu, J. Shi, Y. Li, L. Xu, C. Xie, W. Zhou, Y.C. Huang, T. Wang, S. Du, M. Song, D. Wang, C. Chen, J. Zheng, J. Liu, C.L. Dong, Y. Zou, J. Chen, S. Wang, Activated Ni-OH bonds in a catalyst facilitates the nucleophilic oxidation reaction, *Adv. Mater.* 34 (2022) 2105320.
- [38] H. Xiao, L. Gan, G. Xiao, Z. Qian, W. Rong, H. Guang, J. Bin, X. Chao, P. Fu, Origin of the electrocatalytic oxygen evolution activity of nickel phosphides: in-situ electrochemical oxidation and Cr doping to achieve high performance, *Sci. Bull.* 66 (2021) 708–719.
- [39] L. Di, L. Zeng, Z. Ren, S. Ge, H. Yi, Y. Wu, Y. Wang, L. Chuan, P. Xin, Coupling overall water splitting and biomass oxidation via Fe-doped Ni₂P@C nanosheets at large current density, *Appl. Catal. B: Environ.* 307 (2022), 121170.
- [40] C. Hai, J. Si, X. Bing, H. Cheng, H. Yu, Q. Yan, H. Mao, C. Hai, Sea-urchin-like nickel-cobalt phosphide/phosphate composites as advanced battery materials for hybrid supercapacitors, *J. Mater. Chem. A* 7 (2019) 6241.
- [41] H. Liu, J. Gao, X. Xu, Q. Jia, L. Yang, S. Wang, D. Cao, Oriented construction Cu₃P and Ni₂P heterojunction to boost overall water splitting, *Chem. Eng. J.* 448 (2022), 137706.
- [42] Z.Y. Yu, Y. Duan, X.Y. Feng, X. Yu, M.R. Gao, S.H. Yu, Clean and affordable hydrogen fuel from alkaline water splitting: past, recent progress, and future prospects, *Adv. Mater.* 33 (2021) 2007100.
- [43] B. Zhou, Y. Li, Y. Zou, W. Chen, W. Zhou, M. Song, Y. Wu, Y. Lu, J. Liu, Y. Wang, S. Wang, Platinum modulates redox properties and 5-Hydroxymethylfurfural adsorption kinetics of Ni(OH)₂ for biomass upgrading, *Angew. Chem. Int. Ed.* 60 (2021) 22908–22914.
- [44] B. Zhou, C.L. Dong, Y.C. Huang, N. Zhang, Y. Wu, Y. Lu, X. Yue, Z. Xiao, Y. Zou, S. Wang, Activity origin and alkalinity effect of electrocatalytic biomass oxidation on nickel nitride, *J. Energy Chem.* 61 (2021) 179–185.
- [45] Y. Lu, T. Liu, C.L. Dong, C. Yang, L. Zhou, Y.C. Huang, Y. Li, B. Zhou, Y. Zou, S. Wang, Tailoring competitive adsorption sites by Oxygen-vacancy on cobalt oxides to enhance the electrooxidation of biomass, *Adv. Mater.* 34 (2022) 2107185.
- [46] J. Wu, Understanding the electric double-layer structure, capacitance, and charging dynamics, *Chem. Rev.* 122 (2022) 10821–10859.
- [47] Y. Lu, T. Liu, Y. Huang, L. Zhou, Y. Li, W. Chen, L. Yang, B. Zhou, Y. Wu, Z. Kong, Z. Huang, Y. Li, C. Dong, S. Wang, Y. Zou, Integrated catalytic sites for highly efficient electrochemical oxidation of the aldehyde and hydroxyl groups in 5-hydroxymethylfurfural, *ACS Catal.* 12 (2022) 4242–4251.
- [48] Y. Yang, T. Mu, Electrochemical oxidation of biomass derived 5-hydroxymethyl-furfural (HMF): pathway, mechanism, catalysts and coupling reactions, *Green. Chem.* 23 (2021) 4228–4254.
- [49] Y. Lu, T. Liu, C.L. Dong, Y.C. Huang, Y. Li, J. Chen, Y. Zou, S. Wang, Tuning the selective adsorption site of biomass on Co₃O₄ by Ir single atoms for electrosynthesis, *Adv. Mater.* 33 (2021) 2007056.

- [50] N. Heidary, D. Chartrand, A. Guiet, N. Kornienko, Rational incorporation of defects within Metal-organic frameworks generates highly active electrocatalytic sites, *Chem. Sci.* 12 (2021) 7324–7333.
- [51] X. Deng, G.Y. Xu, Y.J. Zhang, L. Wang, J. Zhang, J.F. Li, X.Z. Fu, J.L. Luo, Understanding the roles of electrogenerated Co^{3+} and Co^{4+} in selectivity-tuned 5-hydroxymethylfurfural oxidation, *Angew. Chem. Int. Ed.* 60 (2021) 20535–20542.
- [52] Y. Song, Z. Li, K. Fan, Z. Ren, W. Xie, Y. Yang, M. Shao, M. Wei, Ultrathin layered double hydroxides nanosheets array towards efficient electrooxidation of 5-hydroxymethylfurfural coupled with hydrogen generation, *Appl. Catal. B: Environ.* 299 (2021), 120669.